Building a representative UAV RGB reference dataset for national-scale satellite mapping of invasive goldenrods (*Solidago* spp.): an efficient workflow and accuracy drivers

Running title: UAV RGB reference data for *Solidago* mapping

Ewa Kołaczkowska[1], Bożena Omeliańska[1]*, Anna Kowalska[1], Martyna Zarzycka[1], Edyta Regulska[1], Anna Jarocińska[2], Marlena Kycko[2], Anna Foks-Ryznar[3], Anna Wawrzaszek[3], Emil Wrzosek[3], Edyta Woźniak[3], Szymon Sala[3], Marek Ruciński[3], Małgorzata Jenerowicz-Sanikowska[3], Andrzej Norbert Affek[1]

[1]Institute of Geography and Spatial Organization, Polish Academy of Sciences, Warsaw, Poland

[2] Faculty of Geography and Regional Studies, University of Warsaw, Warsaw, Poland

[3] Space Research Centre, Polish Academy of Sciences, Warsaw, Poland

*e-mail: **bomelianska@twarda.pan.pl**

Abstract

Reliable wall-to-wall mapping of invasive plants from satellite imagery depends on representative reference data and transparent quality control. Here we present a nationally distributed UAV RGB reference dataset and an end-to-end workflow designed to support

national-scale satellite mapping of invasive goldenrods (*Solidago* spp.) in Poland. During the peak flowering period (August–September 2024), we acquired 79 UAV orthomosaics across environmentally diverse landscapes. Expert interpreters delineated reference polygons for *Solidago* and a background class (other vegetation/land cover) and performed independent visual verification to ensure consistent labelling and to identify recurring sources of confusion. For each orthomosaic we derived a feature stack from RGB imagery (spectral indices and texture metrics) and conducted Random Forest classification, with performance evaluated using class-wise user's accuracy (UA), producer's accuracy (PA), and F1-score. Across sites, *Solidago* classification showed greater variability than the background class and was frequently limited by commission errors, as indicated by comparatively low UA relative to PA. A structured review of spatial error patterns, combined with site-level modelling of logit-transformed accuracy metrics, revealed repeatable operational drivers of false positives. Precision (UA *Solidago*) decreased significantly under stronger direct-sun conditions (higher sun-visibility scores), consistent with increased within-scene contrast, harsh micro-shadows, and occasional glare or specular highlights, which can mimic flowering signals in RGB orthomosaics. Disturbance (mowing) was associated with reduced *Solidago* performance (lower F1 and marginally lower UA), reflecting increased heterogeneity, patch fragmentation, and transitional vegetation states. Deep shadows and woody/shrub contexts showed weaker negative trends, reinforcing their status as high-risk environments requiring intensified visual quality control. We synthesise best-practice recommendations for efficient UAV reference-data acquisition and targeted visual validation, emphasising strategies to minimise false positives and maximise label consistency across a national sampling frame. This workflow provides a practical foundation for robust training and validation of subsequent wall-to-wall satellite mapping of *Solidago* density classes.

Keywords

***Solidago*, drone mapping, RF classification, ground-truth data, invasive species, Poland**

Introduction

Invasive species pose major ecological and economic challenges worldwide. In Poland and across Europe, North American goldenrods (*Solidago* spp.) are among the most problematic invaders (Tokarska-Guzik, 2001; Weber, 2003; Pejchar and Mooney, 2009). Their rapid expansion alters ecosystem processes, displaces native plant communities, and complicates land management (Ledger et al., 2015; Szymura et al., 2016). In Central Europe, invasion is dominated by two species, *S. gigantea* Aiton (giant goldenrod) and *S. canadensis* L. (Canadian goldenrod) (Weber, 1998; Kabuce and Priede, 2010; Szymura and Szymura, 2016a). Both species occupy a broad range of disturbed and semi-natural habitats, particularly fallow lands and ruderal sites, including abandoned farmlands and grasslands, transport corridors, shrub and forest edges, and river valleys (Weber and Jacobs, 2005; Szymura and Szymura, 2016b; Regulska et al., 2026).

Early detection and reliable range mapping are crucial for controlling rapidly spreading invaders and can substantially reduce management costs (Hill et al., 2017). However, at broad spatial scales (e.g., national monitoring), goldenrod research and management are constrained by the scarcity of spatially continuous distribution data. Existing assessments often rely on point observations, which limits large-scale inference and hampers evidence-based policy development (Zagajewski et al., 2024). Because goldenrods can form extensive stands, field surveys alone are rarely sufficient to characterise their distribution and

dynamics across landscapes, creating a need for spatially explicit mapping approaches (Pyšek and Richardson, 2010).

Remote sensing has become a key tool for systematic monitoring of invasive plants (Rakgoale and Ngetar, 2024) and has shown high potential for mapping goldenrod expansion (Rizaludin Mahmud and Hosaka, 2020). Hyperspectral imagery can achieve very high classification performance, but its cost and limited coverage often restrict operational applications (Ishii and Washitani, 2013; Sabat-Tomala et al., 2020, 2022). Multispectral satellite data offer wider coverage and have recently achieved high performance for goldenrod-dominated areas, while accuracy typically decreases in mixed or heterogeneous vegetation (Zagajewski et al., 2024). In this context, UAV-based RGB imagery provides centimetre-scale spatial resolution at comparatively low cost, but with limited spectral information. This makes UAV RGB particularly valuable as a complementary approach for generating high-quality reference data and for diagnosing classification errors in floristically diverse, heterogeneous landscapes.

Goldenrods exhibit broad ecological tolerance, phenotypic plasticity, and the potential for hybridisation, enabling them to occur across a wide range of habitats and vegetation mixtures (Schmid and Bazzaz, 1990; Kabuce and Priede, 2010; Weber and Jacobs, 2005; Szymura et al., 2019; Musiał et al., 2020). These traits, together with habitat heterogeneity and variable illumination conditions, complicate robust remote-sensing detection across large areas, highlighting the importance of carefully designed reference data and quality-control procedures.

Here, we present a nationally distributed UAV RGB reference dataset and an end-to-end workflow designed to support wall-to-wall satellite mapping of invasive goldenrods in Poland. We focus on practical aspects of the multistage task (from survey planning and image acquisition to orthomosaic processing, reference delineation, and classification) and on

identifying repeatable failure modes that influence accuracy. Our goal is to provide actionable best-practice guidance for efficient collection and verification of UAV-derived reference data for goldenrods, with broader relevance to invasive plant monitoring and applied environmental research.

Materials and methods

We describe the study area and the methodological assumptions underlying the workflow used to develop visually verified classifications of invasive goldenrods on UAV-derived orthomosaics (Fig. 1).

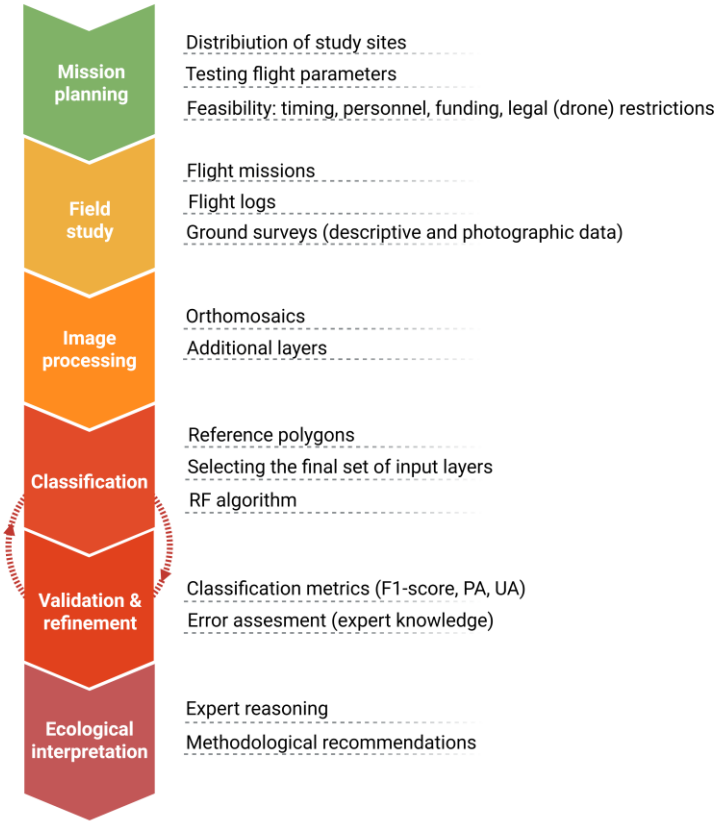

Figure 1. Workflow for mapping goldenrods using UAV-derived RGB orthomosaics.

Study area

We designed the UAV survey and classification to generate a nationally distributed reference dataset suitable for supporting large-scale goldenrod mapping across their invasive range. Our study sites were distributed throughout Poland to capture the variability of habitat types and land-use forms in which goldenrods occur (including regional variability), as well as the morphological and phenological variability of the two dominant invasive goldenrod species in Poland. Efforts were also made to ensure that the study sites were distributed across different Sentinel-2 scenes.

Poland (>300,000 km²) lies predominantly within the humid continental climate zone (Dfb) under the Köppen–Geiger classification (Peel et al., 2007), which also occurs within the native range of North American goldenrods and across large parts of Europe. The national averages of annual precipitation and temperature (based on data from 1991–2020) are 612 mm and 8.7 °C, respectively (IMGW-PIB, 2025). Lowlands (<200 m a.s.l.) cover ~75% of the country and dominate the north and centre, whereas uplands and mountains occur mainly in the south (Fig. 2). Our field sampling targeted agricultural and semi-natural open habitats where goldenrods commonly occur (e.g., fallows and transitional herbaceous–shrub mosaics).

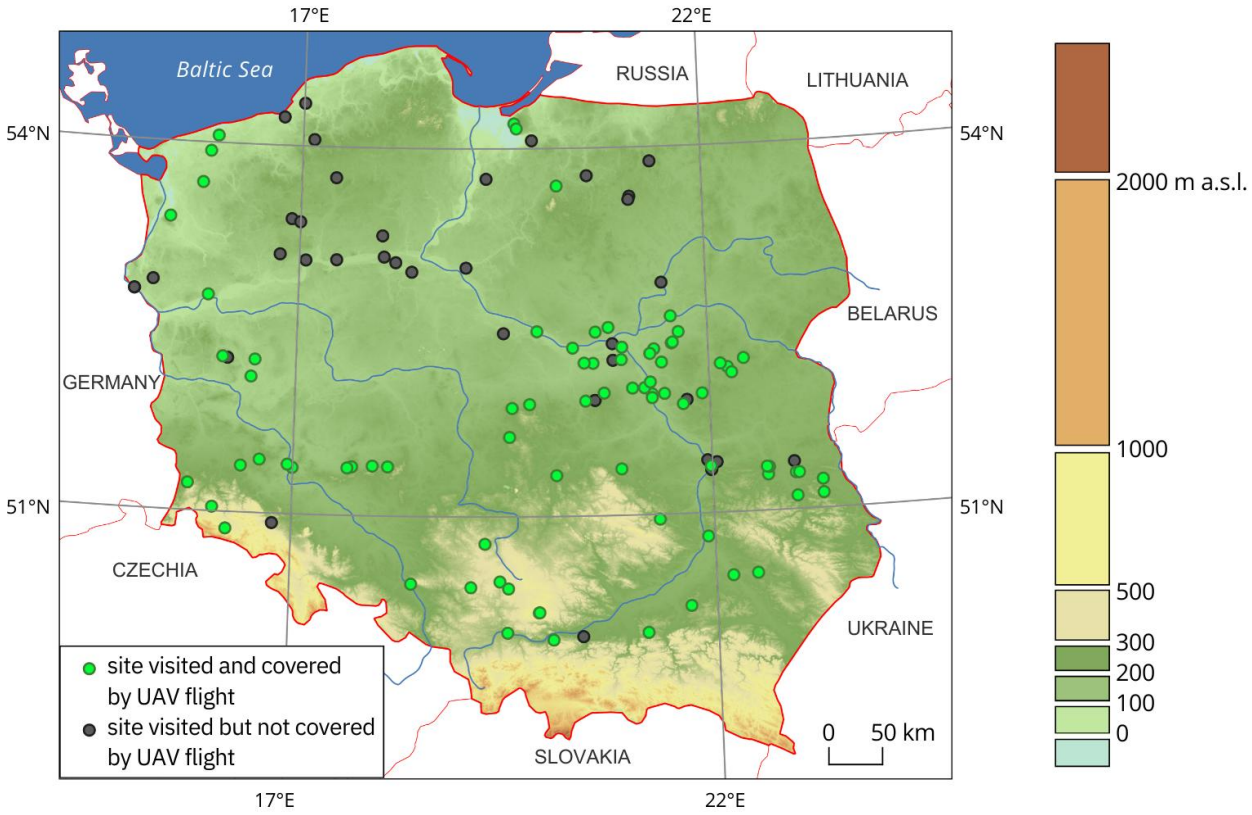

135

136 **Figure 2.** The distribution of study sites across Poland.

137 Mission planning

138 Potential *Solidago* locations were first identified by visual interpretation of Sentinel-2
139 imagery (2023; the year preceding the field campaign), and approximately 1,000 locations
140 were initially selected. Additional spatial context relevant to site selection was consulted
141 using the Geoserwis platform (www.geoserwis.gdos.gov.pl). Sites were then selected to
142 capture a wide range of potentially invaded habitats while maintaining an even spatial
143 distribution across Poland. Ultimately, after additionally considering Sentinel-2 scene
144 coverage to facilitate subsequent satellite-based analyses, regional UAV operating
145 regulations, regional differences in the timing of goldenrod flowering, the duration of the
146 flowering period, and access logistics, approximately 120 locations were selected for field
147 survey.

UAV mapping used a multirotor platform (DJI Matrice 210 RTK V2) equipped with an RGB camera (Zenmuse X5S) and a DJI D-RTK 2 Mobile Station. After testing alternative settings to balance image quality and efficiency, final flight parameters were: altitude 100 m AGL, 70% side overlap, 80% forward overlap, 25% external margin, flight speed 6.5 m s^{-1}, distance-interval shooting, centre-weighted metering, daylight white balance, and Auto Focus Single (AFS) with f/4 aperture. Raw RGB images had a ground sampling distance (GSD) of 2.18 cm and a size of 5280 × 2970 pixels.

Field capacity was constrained by travel logistics, available daylight, and UAV performance. Under optimal conditions, a three-person team (minimum two persons) documented four to six plots per day, travelling ~250 km on average. These operational constraints influenced the final number and distribution of reference sites.

Field study

UAV surveys were conducted from 5 August to 13 September 2024 (31 fieldwork days), timed to the goldenrod flowering period. We conducted 79 UAV missions targeting *Solidago* patches and surrounding vegetation, plus one additional mission documenting vegetation types commonly confused with goldenrods during mission planning. Each *Solidago* mission covered a mean area of 13.93 ha (min = 5.66 ha, max = 30.57 ha), resulting in a total surveyed area of approximately 1,100 ha, with sites distributed throughout Poland (Fig. 2).

We maintained flight logs capturing key parameters (e.g., plot location and dimensions, take-off/landing time, battery levels) and weather conditions (cloud cover, wind gusts). We additionally collected oblique UAV imagery at lower altitude and ground-level photographs and recorded short videos during landing to support subsequent interpretation while optimally using the remaining battery power. Each site was characterised *in situ* by land

cover and land use, goldenrod species identity, abundance, spatial pattern (clumped vs. dispersed), plant height, dominant co-occurring species, and general habitat context. Field data were recorded on a standardized field data sheet developed for this study (Table S1, Supporting information).

We also collected descriptive notes and ground-level photographs at 38 additional planned locations where UAV flights could not be completed, mainly due to adverse weather (precipitation, strong wind), GNSS disruptions (e.g., high geomagnetic activity; Kp ≥ 5), or the sudden activation of temporary flight restriction zones.

Image processing

For each mission, two products were created using Pix4Dmapper, based on nadir images: a high-resolution orthomosaic (2.18 cm) intended for reference delineation, and a downsampled orthomosaic (8.6 cm), produced using Gaussian averaging downsampling, intended for classification.

Reference data processing

Reference data were digitised in QGIS (v3.38.1) on the orthomosaics. For each site, ~100–200 reference polygons were manually delineated to represent two classes: *Solidago* (monospecific invasive goldenrod stands) and Other (background cover including non-*Solidago* vegetation, bare soil, and other surface features). Delineation relied on expert interpretation supported by *in situ* observations. This process required recognising the range of goldenrod morphological forms present at each site (Fig. 3) and identifying potential confusers (Fig. 4). To improve consistency, each polygon set was independently verified by a

botanist (second team member) using oblique UAV imagery, ground-level photographs, and field notes.

invasive goldenrods forming mono- or dispecific patches

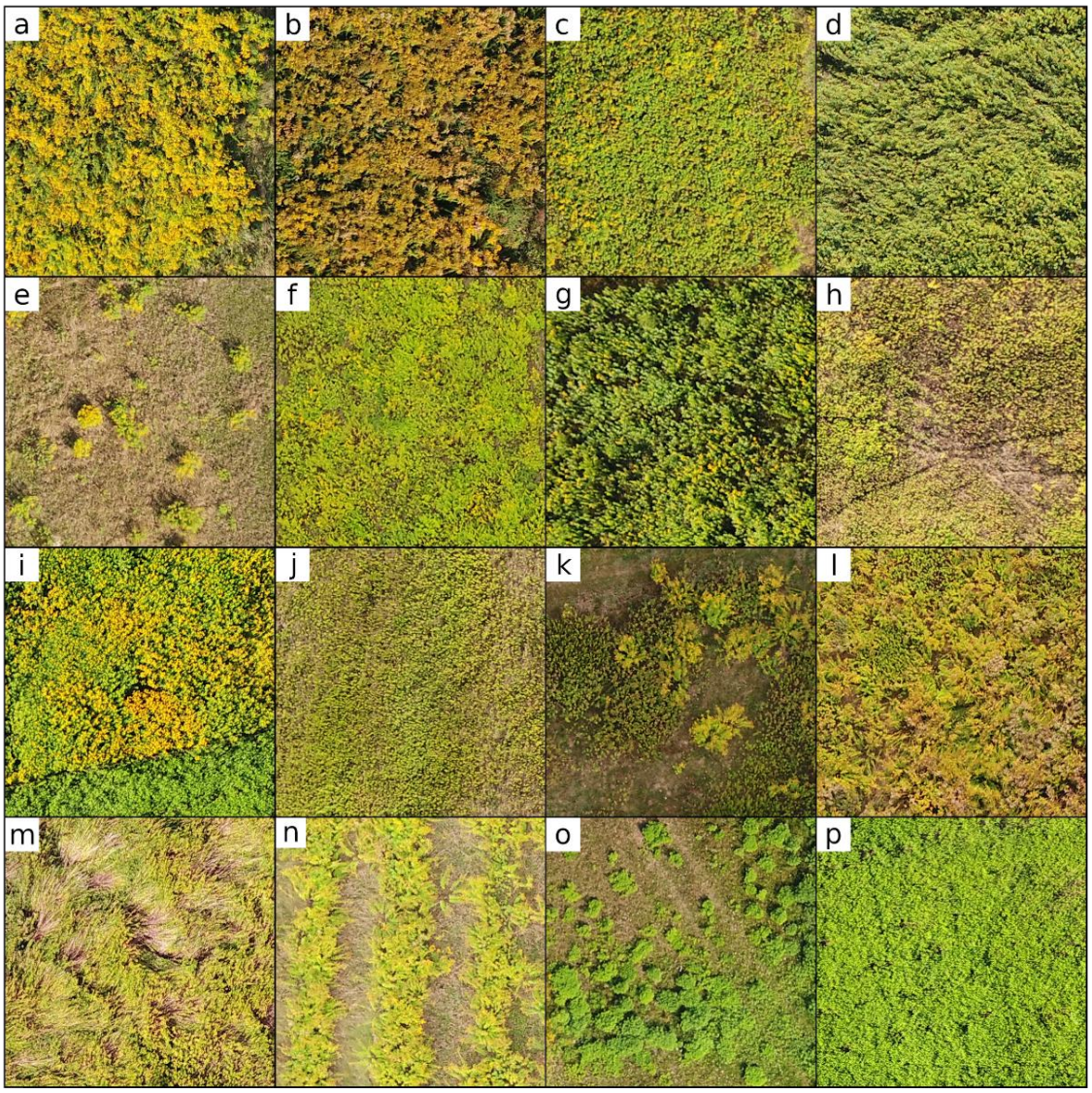

invasive goldenrods mixed with other species

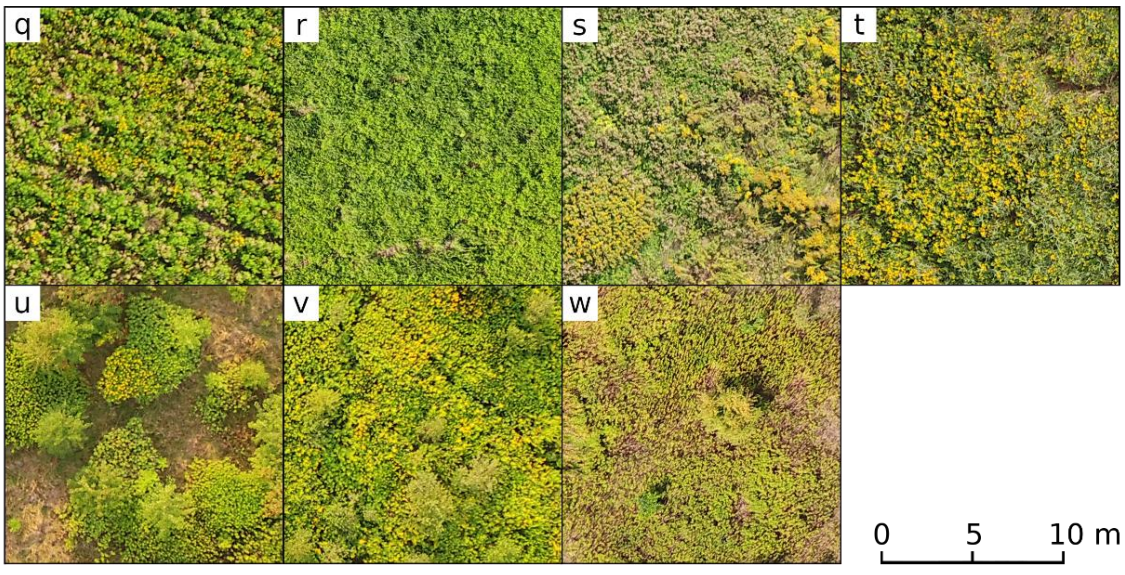

198 **Figure 3.** Examples of the range of morphological forms exhibited by invasive goldenrods in UAV
199 RGB imagery: (a–p) present the examples of goldenrods clearly dominating over other species, so that
200 their morphological diversity results from the species-specific biological traits (*S. gigantea* vs *S.*
201 *canadensis*), combined with site-specific conditions (a–l) and reactions of goldenrods to disturbances
202 (m–p); (q–w) the common examples of goldenrod populations coexisting with the species of similar
203 shape and/or colour; (a) high and dense, fully blooming *S. canadensis* ramets in Pabianice (27 Aug);
204 (b) high and dense, fading *S. canadensis* ramets in Elbląg-2 (5 Sep); (c) short and dense, partly
205 blooming *S. gigantea* ramets in Hredków (29 Aug); (d) tall and dense, fading *S. gigantea* ramets in
206 Nowy Kamion (3 Sep); (e) goldenrods growing in clumps at the edge of the main colony in Hredków
207 (29 Aug); (f) a mosaic of flowering *S. gigantea* and pre-flowering *S. canadensis* ramets in Gryfice
208 (Aug 22); (g) *S. gigantea* ramets growing on a histosol in Czeszów (6 Aug); (h) short *S. gigantea*
209 ramets growing on an arenosol in Wólka Pęcherska (11 Sep); (i) blooming *S. gigantea* and *S.*
210 *canadensis* ramets adjacent to the mowed southern part of the colony (with regenerating juvenile
211 shoots) in Czeszów (6 Aug); (j) short, mostly non-flowering *S. gigantea* ramets growing on a fluvisol
212 containing sand deposits in the Vistula valley in Płock (3 Sep); (k) a mosaic of evenly distributed *S.*
213 *gigantea* ramets interspersed with clumps of *S. canadensis* in Bogdaniec (9 Sep); (l) co-occurring *S.*
214 *gigantea* and *S. canadensis* in Doliwo, presenting different flowering stages and distribution patterns
215 (12 Sep); (m) tall goldenrod shoots lodged by animal trampling in Osieck (11 Sep); (n) *S. canadensis*
216 ramets growing in stripes in the abandoned field (former permanent crop) in Doliwo (12 Sep); (o)
217 clumps of juvenile goldenrods regenerating after mowing in Hredków (29 Aug); (p) evenly
218 distributed, juvenile goldenrod shoots, regenerating after mowing in Czeszów (6 Aug); (q) juvenile
219 goldenrod shoots (green) mixed with *Tanacetum vulgare* L. (yellow) and *Erigeron canadensis* L.
220 (beige) in Nowa Kuźnia (7 Aug); (r) juvenile goldenrod shoots (light green) mixed with grasses
221 (green) in Czeszów (6 Aug); (s) flowering and partly faded *S. gigantea* and *S. canadensis* (yellowish)
222 mixed with faded *Eupatorium cannabinum* L. (beige) in Głębokie (29 Aug); (t) flowering goldenrods
223 mixed with *Phragmites australis* (Cav.) Trin. ex Steud. in Szczecin (22 Aug); (u) and (v) goldenrods
224 mixed with *Acer negundo* L. (short trees with bushy, yellowish crowns), both in Dłużyna Górna (7
225 Aug); (w) goldenrods mixed with *Prunus cerasifera* Ehrh. (shrubs or short trees) in Osieck (11 Sep);

all the images were captured by the authors during the field study in Poland in 2024 (flight altitude: 100 m AGL, GSD: 2.18 cm); detailed information on the image locations is provided in Table S2 (Supporting information), and corresponding ground-level photographs for selected images are presented in Figs. S1–S11 (Supporting information).

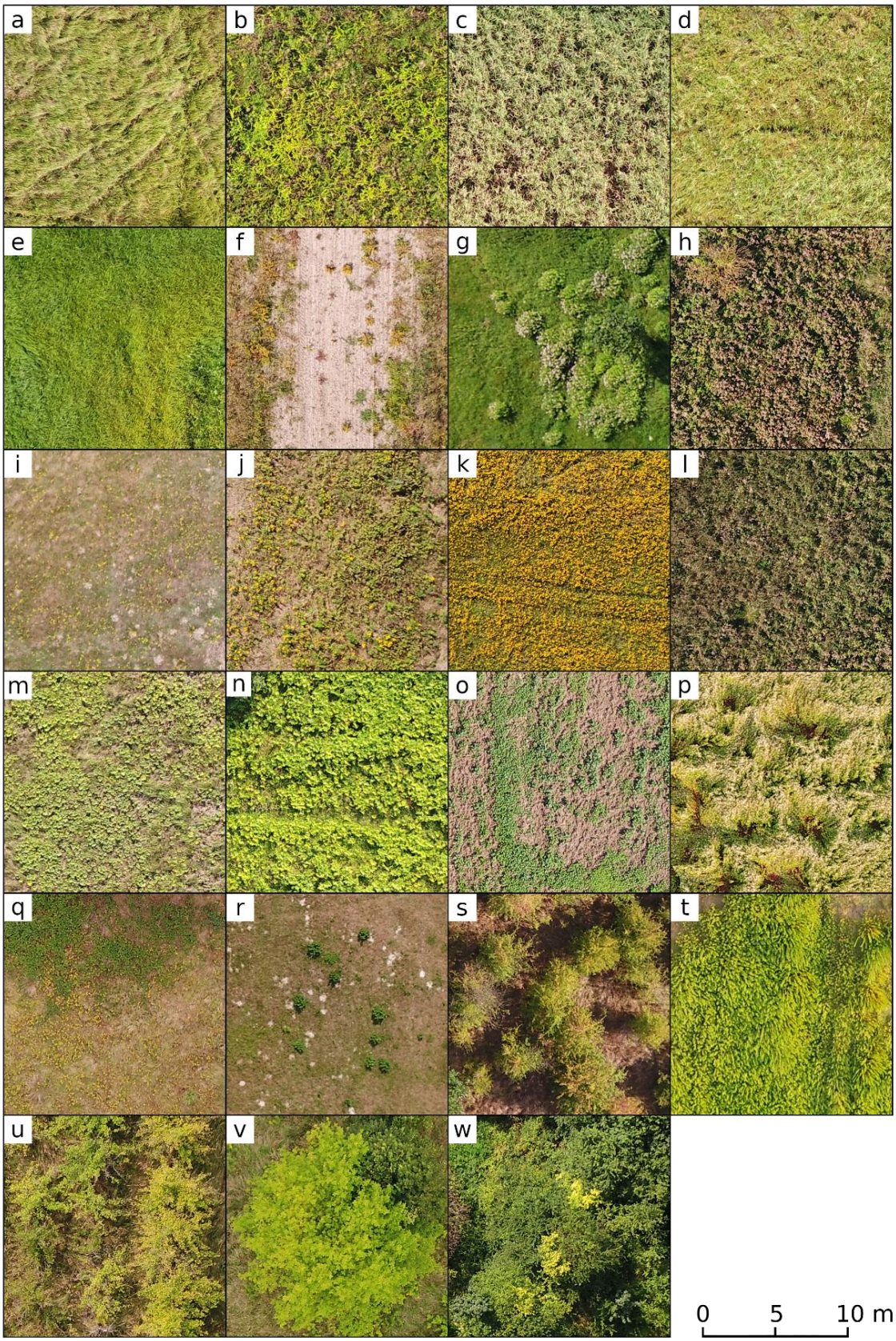

Figure 4. Examples of vegetation that is visually similar to invasive goldenrods in UAV RGB imagery and may cause misclassification if not represented in the reference dataset: (a–e) graminoids,

(f–p) forbs, (q–w) shrubs and trees; (a) lodged tall grass shoots in Częstochowa (10 Aug); (b) clumps of maize in Nowa Kuźnia (7 Aug); (c) reeds in Częstochowa (10 Aug); (d) reeds mixed with grasses in Częstochowa (10 Aug); (e) grasses mixed with sedges in Kopanica (24 Aug); (f) clumps of knotweeds on fallow land in Kłudno (27 Aug); (g) clumps of flowering *Eupatorium cannabinum* L. on a pasture in Tarnowskie Góry (9 Aug); (h) extensive clumps of fruiting *E. cannabinum* (beige pappus) mixed with small trees in Hredków (29 Aug); (i) scattered individuals of native to Europe *Solidago virgaurea* L. (yellow), accompanied by lichens (grey) and drought-tolerant grasses (grey-green) in Bogdaniec (9 Sep); (j) flowering in yellow *Tanacetum vulgare* L. mixed with arable weeds, mostly *Erigeron canadensis* L. (light green) in Krępna (9 Aug); (k) flowering in yellow hawksbeards (*Crepis* L.) in Czubrowice-2 (13 Aug); (l) fruiting thistles (*Cirsium* L.), beige colour of the pappus, mixed with grasses in Hredków (29 Aug); (m) *Petasites hybridus* (L.) P. Gaertner, B. Meyer et Scherb. (large, rounded, yellowish leaves) in Płock (3 Sep); (n) an extensive patch of invasive *Heracleum sosnowskyi* Manden. in Siewierz (10 Aug); (o) winter oilseed rape (*Brassica napus* L.) growing in a field in Dziekanów Polski (3 Sep); (p) a lodged field of common buckwheat (*Fagopyrum esculentum* Moench) in Dłużyna Górna (7 Aug); (q) bramble (*Rubus fruticosus* agg.) thickets (dark green leaves, occur mostly in the northern part of the image) and flowering in yellow *Lysimachia vulgaris* L. individuals (occur mostly in the southern part of the image) in Doliwo (12 Sep); (r) juvenile black alder (*Alnus glutinosa* (L.) Gaertn.) expanding across an abandoned meadow in Głębokie (29 Aug); (s) small and short trees from the rose family (Rosaceae) in Garwolin (11 Sep); (t) a willow plantation in Zbąszyń (23 Aug); (u) juvenile *Acer negundo* trees, self-sown in rows within a former orchard, replacing former fruit trees, in Gorzów (23 Aug); (v) a mature *A. negundo* tree (light green) resembling a dense goldenrod patch in Gryfice (22 Aug); (w) a willow thicket in Tarnowskie Góry (9 Aug); all the images were captured by the authors during the field study in Poland in 2024 (flight altitude: 100 m AGL, GSD: 2.18 cm); detailed information on the image locations is provided in Table S2 (Supporting information), and corresponding ground-level photographs for selected images are presented in Figs. S1–S11 (Supporting information).

Derivation of additional layers and classification

To improve class separability, we supplemented RGB orthomosaics with spectral indices and textural features, which can enhance detection of subtle spectral and structural differences (e.g., Biró et al., 2024). The final input feature set comprised a RGB orthomosaic, selected spectral indices, and GLCM-based texture layers (see Table S3). Texture features were computed using Gray Level Co-occurrence Matrix (GLCM) metrics following Haralick et al. (1973). Both texture features and spectral indices were derived from the 8.6 cm orthomosaic, which was also used for classification. GLCM texture metrics (contrast, entropy, homogeneity) were computed separately for each RGB channel using a 3×3 moving window.

Orthomosaics were classified using Random Forest (Breiman, 2001) via an automated workflow in R (v4.2.2; R Core Team, 2022). Spatial processing was performed using the *raster*, *terra*, and *sf* packages. Texture features and spectral indices were computed using *glcm* and *terra*. Classification employed *randomForest*, *caret*, and *e1071*, with parallel processing via *foreach*, *doParallel*, and *doRNG*. Data handling and export were carried out using *tidyverse* (including *dplyr* and *tidyr*) and *openxlsx*.

Pixel-level samples were extracted from the reference polygons and randomly divided, with 50% allocated for training and 50% for validation. This split was designed to evaluate classification reliability within each orthomosaic for reference-data generation, rather than transferability across sites. Models were trained with 500 trees, and classification was repeated 10 times to account for sampling variability.

Performance evaluation

Performance was evaluated using Producer's Accuracy (PA), User's Accuracy (UA), and F1-score, and prediction maps were subsequently subjected to expert visual verification.

To assess whether classification errors were dominated by false positives or false negatives, we quantified error asymmetry using a site-level dominance index for the *Solidago* class defined as PA − UA. Because PA decreases with increasing false negatives and UA decreases with increasing false positives, positive values indicate a relatively stronger influence of false positives, whereas negative values reflect a relatively stronger impact of false negatives.

Dominance indices were calculated for all sites and tested against zero using the Wilcoxon signed-rank test. The same test was applied to subsets of best- and worst-classified orthomosaics. Differences between these subsets were assessed using the Mann–Whitney U test. All tests were two-sided and non-parametric. Analyses were performed in IBM SPSS Statistics (v30).

To complement qualitative error diagnostics, we modelled whether acquisition and scene characteristics explain between-site variability in *Solidago* performance. Two response variables were analysed at the site level: (i) UA (precision; linked to false positives) and (ii) F1-score (overall performance). Because UA and F1 are bounded in (0,1), we applied a logit transformation (after trimming any 0/1 values if present) and fitted separate multiple linear regression models on the logit scale.

Candidate predictors were defined a priori and included: shade cover (%), cloud cover (0–1, rescaled from the octas scale 0–8), sun visibility (ordinal field score; 1 = sun not visible/overcast, 5 = sun fully visible for most of the mission), deciduous tree and shrub cover (%), mown/disturbed area (%), mission start time, and days since the first UAV flight (phenology proxy). Percentage predictors were visually estimated from orthomosaics, while remaining predictors were obtained from flight logs (Table S2, Supporting information). We also included a simple time-of-day proxy for solar geometry: distance from approximate solar

noon (SolarNoonDist_h, hours), computed as the absolute difference between mission start time (decimal hours) and 13.25 (13:15 CEST): SolarNoonDist_h = |t_start − 13.25|.

All subsets of candidate predictors were compared using Akaike Information Criterion corrected (AICc). Multicollinearity in retained models was assessed using Variance Inflation Factor (VIF), and assumptions were evaluated using residual diagnostics (IBM SPSS Statistics v30). Regression effects were reported as coefficients with confidence intervals on the logit scale and interpreted in terms of expected influence on false positives (UA) and overall performance (F1-score).

Results

Overall classification performance

Across the 79 orthomosaics, classification performance was consistently high for the Other class (mean F1 = 0.948 ± 0.031), whereas performance for *Solidago* was lower and more variable (mean F1 = 0.873 ± 0.070; Fig. 5). The higher variability in *Solidago* F1 indicates that detection of invasive goldenrods was more sensitive to site-specific conditions and scene characteristics than background classification.

For the Other class, more than half of orthomosaics exceeded F1 = 0.950 (Fig. 5). In contrast, *Solidago* F1 values were more broadly distributed, most frequently falling in the 0.900–0.950 and 0.850–0.900 ranges, with ~15% of sites below 0.800 (Fig. 5).

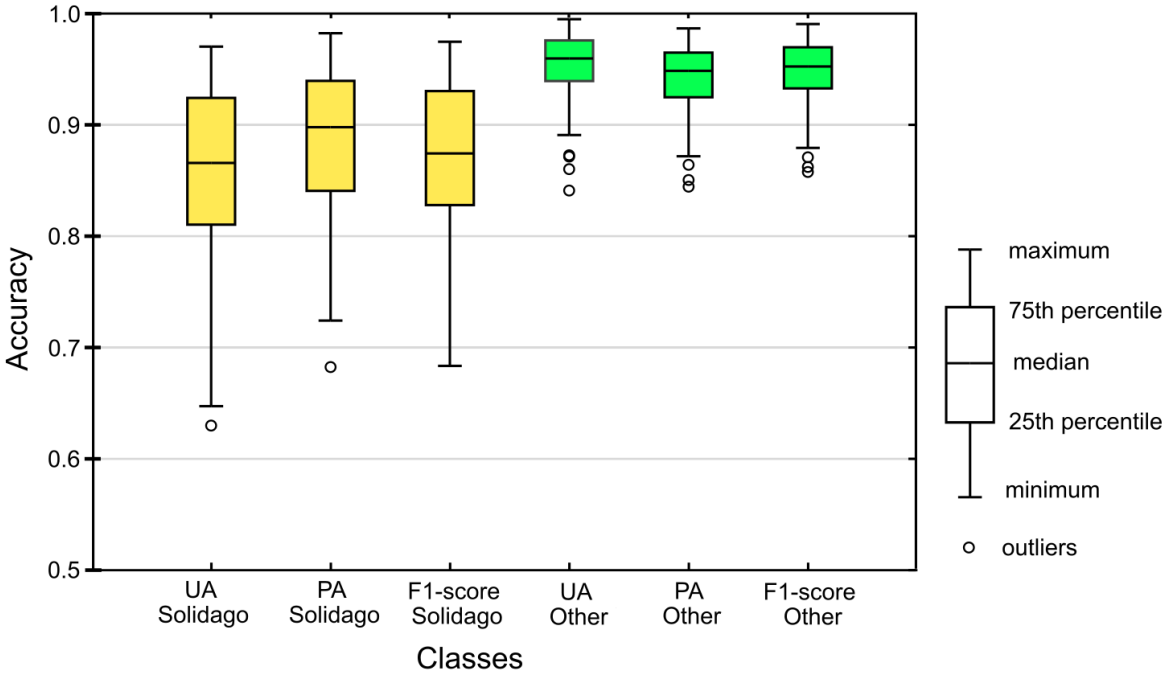

Figure 5. Accuracy measures for all classified orthomosaics (N = 79).

Best- and worst-classified orthomosaics and error asymmetry

The highest *Solidago* performance (F1 ≥ 0.950) occurred in ten orthomosaics (Table 1). These sites were characterised by dense, homogeneous goldenrod patches, limited presence of visually similar vegetation, and clear textural contrast, yielding high and balanced UA and PA (both >0.926).

The lowest *Solidago* performance occurred in Nowa Kuźnia (F1 = 0.684), Bogdaniec (F1 = 0.703), and Częstochowa (F1 = 0.719), where goldenrods were sparse or patchy, vegetation structure was heterogeneous, or goldenrods were poorly separable from co-occurring species (Table 2).

Table 1. Accuracy metrics for the best-classified orthomosaics (F1 *Solidago* > 0.950 and F1 Other > 0.970) and selected site characteristics.

Site name	Date	UA *Solidago*	PA *Solidago*	F1 *Solidago*	F1 Other

Zgierz	26 Aug	0.967	0.982	0.975	0.982
Wola Rzędzińska	14 Aug	0.965	0.979	0.972	0.982
Liszno-Kolonia	28 Aug	0.963	0.974	0.969	0.989
Łuszczów Pierwszy	28 Aug	0.970	0.967	0.968	0.981
Naborów	9 Sep	0.969	0.961	0.965	0.977
Domasławice	6 Aug	0.953	0.973	0.963	0.987
Świebodzin	23 Aug	0.950	0.969	0.959	0.968
Błędów	9 Sep	0.959	0.959	0.959	0.980
Włodzimierzów	27 Aug	0.928	0.980	0.953	0.987
Głębokie	29 Aug	0.926	0.976	0.951	0.982

Across all sites, dominance indices for *Solidago* (PA − UA) were significantly greater than zero (median = 0.028; Wilcoxon signed-rank test, $p < 0.001$), indicating that false positives tended to contribute more strongly than false negatives to classification error. This tendency was weak but still detectable among the best-classified orthomosaics (median = 0.014; $p < 0.05$; Table 1) but was markedly stronger among the worst-classified orthomosaics (median = 0.059; $p < 0.01$; Table 2). Dominance indices differed significantly between the best and worst groups (Mann–Whitney $U = 31.0$, $p = 0.024$), confirming that classification failures in poorly performing sites were driven primarily by false alarms rather than missed detections.

353 **Table 2.** Accuracy metrics for the worst-classified orthomosaics (F1 *Solidago* < 0.810) and selected
354 site characteristics. Classification results for all mapped sites are provided in Table S2 (Supporting
355 information).

Site name	Date	UA *Solidago*	PA *Solidago*	F1 *Solidago*	F1 Other	Main challenges*
Nowa Kuźnia	7 Aug	0.647	0.724	0.684	0.912	*habitat_diver*, *mowing*, *non-flowering*, *flowering*, *fruiting*
Bogdaniec	9 Sep	0.677	0.731	0.703	0.943	*many_Sol_spec*, *flowering*, *fruiting*
Częstochowa	10 Aug	0.630	0.838	0.719	0.974	*many_Sol_spec*, *habitat_diver*, *non-flowering*, *flowering*
Krępna	9 Aug	0.652	0.855	0.740	0.967	*many_Sol_spec*, *habitat_diver*, *non-flowering*, *flowering*
Podkampinos	9 Sep	0.819	0.682	0.745	0.881	*many_Sol_spec*, *flowering*
Ścinawa	7 Aug	0.718	0.806	0.760	0.953	*many_Sol_spec*, *habitat_diver*, *non-flowering*, *flowering*
Czersk	30 Aug	0.734	0.797	0.764	0.933	*many_Sol_spec*, *habitat_diver*, *wind_trampl*, *flowering*, *lodged*
Wólka Pęcherska	11 Sep	0.718	0.826	0.769	0.881	*many_Sol_spec*, *flowering*, *lodged*
Garwolin	11 Sep	0.814	0.752	0.782	0.930	*mowing*, *flowering*,

						juveniles
Dziekanów Polski	3 Sep	0.766	0.805	0.785	0.932	*habitat_diver, wind_trampl, non-flowering, flowering*
Czubrowice-2	13 Aug	0.740	0.839	0.787	0.952	*habitat_diver, non-flowering, mowing, flowering, juveniles*
Tarnowskie Góry	9 Aug	0.770	0.824	0.796	0.916	*habitat_diver, non-flowering, flowering, juveniles, lodged*
Chruszczobród	9 Aug	0.782	0.835	0.808	0.928	*habitat_diver, mowing, non-flowering, flowering, juveniles*
Osieck	11 Sep	0.810	0.805	0.808	0.862	*habitat_diver, wind_trampl, non-flowering, flowering, lodged*

* Main challenges in goldenrod detection include morphological variability resulting from the co-occurrence of multiple goldenrod species (*many_Sol_spec*), high (micro)habitat diversity (*habitat_diver*), and disturbances such as mowing (*mowing*) and wind or trampling (*wind_trampl*), as well as the co-occurrence of plants resembling specific morphological forms of goldenrod shoots, including those resembling non-flowering shoots (*non-flowering*), flowering shoots (*flowering*), fruiting shoots (*fruiting*), regenerating juvenile shoots after mowing (*juveniles*), and lodged shoots due to disturbances or the weight of inflorescences (*lodged*). Examples of goldenrod morphological variability and visually similar plant species are shown in Figs. 3–4 and Figs. S1–S11 (Supporting information).

Two representative worst-classified cases (Osieck and Czubrowice-2; Figs. 6–7) illustrate distinct mechanisms of *Solidago* overestimation. At Osieck (F1 *Solidago* = 0.808), fragmented goldenrod occurrence and high structural heterogeneity reduced class separability,

leading to confusion with structurally similar forbs, graminoids, and locally with woody vegetation (Table 2; Fig. 6). At Czubrowice-2, extensive flowering of visually similar yellow-flowering vegetation resulted in substantial false positives and pronounced overestimation of the *Solidago* class (Table 2; Fig. 7). Importantly, even in sites with low F1 *Solidago*, the Other class typically remained well classified (F1 ≥ 0.881; Table 2), indicating that most errors were confined to the target class rather than reflecting broader mapping failure.

Figure 6. Case study from Osieck illustrating *Solidago* overestimation by the Random Forest classifier: (a) UAV-derived RGB orthomosaic; (b) orthomosaic overlaid with the classification result (*Solidago* class shown in yellow); (c) enlarged detail showing an area without invasive goldenrods (cyan outline) that was misclassified as *Solidago*, including birch crowns (light-green leaves, relatively smooth texture), flattened sedges, and adjacent herbaceous field vegetation.

Figure 7. Case study from Czubrowice-2 illustrating false positives driven by confusion with co-flowering vegetation: (a) UAV-derived RGB orthomosaic; (b) orthomosaic overlaid with the classification result (*Solidago* class shown in yellow); (c–d) enlarged details showing areas without invasive goldenrods (cyan outlines) where yellow-flowering meadow species (*Crepis* sp.) and arable weeds were misclassified as *Solidago*.

Drivers of false positives (*Solidago* precision)

In the site-level regression for UA *Solidago* (logit-transformed), the AICc-selected model retained four predictors: mowing/disturbance cover, sun visibility, deciduous shrubs/trees cover, and mission start time (Table 3). The model explained a moderate proportion of between-site variability ($R^2 = 0.183$; adjusted $R^2 = 0.139$) and was statistically significant ($F_{4, 74} = 4.15$, $p = 0.004$).

Sun visibility showed a significant negative association with UA ($p = 0.012$), indicating lower precision under stronger direct sunlight (higher field scores). This pattern is consistent with increased within-scene contrast and harsher illumination conditions, which may lead to inflated false positives in UAV RGB orthomosaics. Mowing/disturbance cover was also negatively associated with UA ($p = 0.052$), and deciduous shrubs/trees cover showed a weaker negative trend ($p = 0.094$), whereas mission start time was not significant ($p = 0.114$). Multicollinearity was negligible (VIF ≤ 1.02; Table 3).

Drivers of overall *Solidago* performance

In the regression analysis for *Solidago* F1-score (logit-transformed), the AICc-selected model retained disturbance (mowing) cover and shade cover (Table 3). Explanatory power was modest ($R^2 = 0.072$; adjusted $R^2 = 0.048$), and the overall model was marginally significant ($F_{2,76} = 2.96$, $p = 0.058$).

Disturbance (mowing) cover showed a significant negative association with *Solidago* F1 ($p = 0.037$), whereas shade cover exhibited the expected negative trend but was not significant ($p = 0.125$). Multicollinearity was negligible (VIF ≈ 1.03; Table 3).

Table 3. Site-level drivers of *Solidago* classification performance (logit-transformed UA and F1-score).

Response (logit-transformed)	AICc-selected predictors retained	Model fit	Predictor	B (SE)	Std. β	95% CI for B	p	VIF
F1 *Solidago*	Shade cover [%], Disturbances (mowing) [%]	$R^2 = 0.072$; Adj. $R^2 = 0.048$; F(2, 76)=2.963; p=0.058; RMSE=0.689	Intercept	2.368 (0.139)	—	[2.092, 2.644]	<0.001	—
			Shade cover [%]	−0.016 (0.010)	−0.174	[−0.037, 0.005]	0.125	1.031

			Disturbances (mowing) [%]	**−0.012 (0.006)**	**−0.238**	**[−0.023, −0.001]**	**0.037**	1.031
UA *Solidago*	Disturbances (mowing) [%], Sun visibility (1–5), Deciduous trees and/or shrubs [%], Mission start time	R^2 = 0.183; Adj. R^2 = 0.139; F(4, 74)=4.146; p=0.004; RMSE=0.678	Intercept	2.227 (0.443)	—	[1.344, 3.110]	<0.001	—
			Disturbances (mowing) [%]	−0.011 (0.006)	−0.210	[−0.022, 0.000]	0.052	1.022
			Sun visibility (1–5)	**−0.140 (0.054)**	**−0.274**	**[−0.249, −0.032]**	**0.012**	1.018
			Deciduous trees and/or shrubs [%]	−0.012 (0.007)	−0.179	[−0.026, 0.002]	0.094	1.008
			Mission start time	1.306E−5 (0.000)	0.169	[0.000, 0.000]	0.114	1.009

Discussion

Recent reviews indicate growing use of UAVs and machine learning for invasive plant monitoring, but also highlight a lack of methodological standardisation, particularly in how reference data are designed and quality-controlled (Singh et al., 2024). Our study contributes a nationally distributed UAV RGB reference dataset and a comprehensive end-to-end workflow, integrating expert delineation, automated classification, and checklist-based visual verification. This combination proved essential for producing reference data that are both numerically accurate and ecologically meaningful across heterogeneous landscapes, and aligns with broader evidence that well-structured, ground-truth reference data remain critical in habitat mapping workflows (Kvile et al., 2024), particularly in dynamically changing vegetation mosaics such as those shaped by invasive species spread (Akandil et al., 2021; Koco et al., 2021).

Error structure and the value of visual quality control

Across sites, classification performance was generally satisfactory; however, our results show that errors in *Solidago* mapping are systematically biased toward false positives, especially in poorly performing orthomosaics. This implies that model failure is more often driven by false alarms than under-detection, an important distinction for monitoring and management. In early detection contexts, false positives primarily increase the need for field verification, whereas false negatives risk overlooking invasion hotspots. Conversely, for planning control interventions, false positives can inflate estimated invaded area and misdirect resources. The dominance index (PA − UA) provides a simple and robust diagnostic of error asymmetry that complements conventional accuracy metrics and supports more management-relevant interpretation of classifier behaviour.

Standard accuracy statistics alone do not fully capture the ecological context of misclassifications. We therefore strongly recommend systematic visual inspection of reference polygons and prediction maps, particularly when outputs are intended for management or as training data for subsequent wall-to-wall satellite mapping. In our workflow, visual verification served three roles: (i) improving label consistency by cross-checking polygon delineation against oblique UAV imagery, ground photographs, and field notes; (ii) identifying recurring confusers and scene contexts associated with false positives; and (iii) distinguishing isolated mapping artefacts from ecologically plausible *Solidago* patterns. This step was critical for refining the reference dataset and for translating accuracy metrics into actionable guidance (Akandil et al., 2021).

Drivers of performance and repeatable failure modes

Between-site variability in accuracy highlights the combined importance of habitat structure, patch density, and visual distinctiveness of *Solidago* stands. As in previous UAV-based

studies of invasive plants (e.g., de Sá et al., 2018; Hill et al., 2017; Bolch et al., 2020; Singh et al., 2024), performance was highest in sites where *Solidago* formed dense, homogeneous patches and lowest in mixed or transitional vegetation. Although surveys were timed to the flowering period, often considered optimal for goldenrod discrimination (Nowak et al., 2018; Koco et al., 2021; Chadoulis et al., 2023), flowering alone did not eliminate uncertainty. Previous work has emphasised practical limits to remote detection when target plants occur under dense canopies or are heavily modified by disturbance (e.g., mowing, grazing, spraying) (Dvořák et al., 2015; Müllerová et al., 2017). In our study, multiple morphological forms of goldenrods (driven by species traits, site moisture and soils, and disturbances such as mowing or trampling) increased within-class variability, while co-occurring vegetation with similar colour and texture complicated both reference delineation and classification.

Disturbance (mowing) emerged as a consistent limitation: it reduced overall *Solidago* performance (lower F1) and tended to reduce precision (lower UA). This supports the mechanistic interpretation that disturbed mosaics increase heterogeneity, fragment patches, and create transitional vegetation states that amplify both omission and commission errors, consistent with prior UAV-based invasive plant studies reporting performance drops in disturbed or heterogeneous vegetation (Akandil et al., 2021; Koco et al., 2021). In addition, precision decreased significantly under stronger direct sunlight (higher sun-visibility scores), consistent with increased within-scene contrast, harsh micro-shadows, and occasional specular reflections in RGB orthomosaics that can inflate false positives.

Confusers and contextual effects

Visual inspection revealed a broad set of confusers, including other invasive taxa (e.g., *Acer negundo* L., *Reynoutria japonica* Houtt., *Heracleum sosnowskyi* Manden.) and native expansive or pioneer vegetation (e.g., graminoids, reeds, nettles, brambles, willows and

birch), as well as some crops. Notably, many false positives were associated not with yellow flowers but with light-green or late-summer yellowing foliage of herbaceous vegetation and low woody plants. The weaker-than-expected effect of woody cover in the regression models likely reflects the use of simple percentage cover metrics, which do not capture the spatial arrangement of shrubs/trees (e.g., edges, isolated clumps, shadow geometry) that drives visual confusion.

Implications for best practice and transferability

Our observations support several practical recommendations for UAV-based reference-data collection aimed at minimising false positives. First, where feasible, UAV surveys should be conducted under diffuse illumination and stable exposure conditions. Second, recently disturbed or mown areas should be explicitly identified and either stratified during sampling or prioritised for denser reference delineation and stricter validation, given their consistently lower performance. Third, structurally heterogeneous environments, particularly shrub and forest edges, should be treated as high-risk contexts requiring enhanced visual quality control.

Planning should also account for seasonal anomalies (Lu and He, 2017). Drought can accelerate senescence and leaf yellowing, extending periods when non-target vegetation resembles flowering goldenrods, especially in abandoned agricultural mosaics with shrubs and low trees. Conversely, missions early in the flowering season can increase confusion with common yellow-flowering species (e.g., *Tanacetum vulgare* L.) and with rapidly regenerating graminoids after mowing. Overall, the reliability of UAV-derived reference data depends on consistent execution and expert oversight across all workflow stages. We therefore recommend involving botanical expertise not only during fieldwork but throughout reference delineation and output verification, ideally within a small, consistent team to maintain methodological continuity.

Conclusions

This study demonstrates that systematically planned and executed UAV RGB surveys, with countrywide distribution, can provide an efficient and highly informative reference dataset for national-scale satellite mapping of invasive goldenrods (*Solidago* spp.), while underscoring the indispensable role of expert visual inspection at multiple stages of the workflow. High-resolution orthomosaics enable interpretable, vegetation-structure–aware delineation of *Solidago* patches; however, automated classification alone cannot guarantee reliable reference labels or stable performance across environmentally diverse sites. A structured protocol for visual verification of vegetation and mapped outputs is therefore a core requirement for scaling reference-data collection.

Beyond summary accuracy metrics, combining class-wise UA/PA/F1 with systematic visual review of spatial error patterns yields actionable diagnostic insight. In particular, the workflow reveals that commission errors (false positives) are a recurrent limitation in *Solidago* detection and should be treated as a primary quality-control target. False positives tend to cluster in predictable scene contexts, making targeted visual checks more effective than relying on overall accuracy alone. The quantitative driver analysis supports and clarifies visually observed mechanisms. Stronger direct-sun conditions (higher sun-visibility scores) were associated with lower precision (UA *Solidago*), consistent with increased within-scene contrast, harsh micro-shadows, and occasional glare/specular highlights in RGB orthomosaics that can mimic bright flowering signals. Recent disturbance (mowing) was linked to reduced *Solidago* performance (lower F1 and marginally lower precision), and visual inspection confirms why: disturbed mosaics increase heterogeneity, fragment patches, and create transitional vegetation states that amplify confusion. Deep shadows and woody/shrub

contexts showed weaker but consistent negative trends, reinforcing their status as high-risk environments that require intensified visual quality control and, where needed, denser reference delineation.

Overall, the most scalable pathway to reliable UAV-derived reference data is not full automation but an integrated workflow: standardised acquisition and metadata capture, expert delineation, automated classification, and targeted, visual validation focused on known failure modes to minimise false positives and maximise consistency across a national sampling frame.

Supporting information

Table S1. Field data sheet (consisting of three consecutive pages) used for the field survey.

Table S2. Selected properties of UAV-mapped sites during the field study across Poland in 2024 and the results of RF-classification of the orthomosaics.

Table S3. Spectral indices and GLCM-based texture metrics used as additional predictor layers for Random Forest classification of the UAV-derived RGB orthomosaics.

Figures S1–S11. Ground-level photographs supplementing Figures 3–4, and Table 2

Acknowledgements

This study was funded by Poland's Ministry of Science and Higher Education under the Science for Society Programme (grant No. NdS-II/SP/0216/2024/01).

Author Contributions

Ewa Kołaczkowska: conceptualization, data curation, formal analysis, investigation, methodology, project administration, resources, supervision, validation, visualisation, writing – original draft, writing – review and editing; **Bożena Omeliańska:** conceptualization, data curation, formal analysis, investigation, methodology, software, visualisation, writing – original draft; **Anna Kowalska:** investigation, project administration, validation, writing – original draft, writing – review and editing; **Martyna Zarzycka** investigation, project administration, validation, writing – review and editing; **Edyta Regulska:** validation, visualisation, writing – original draft, writing – review and editing; **Anna Jarocińska:** conceptualization, formal analysis, methodology, visualisation, writing – review and editing; **Marlena Kycko:** conceptualization, methodology; **Anna Foks-Ryznar:** methodology, resources, writing – original draft, writing – review and editing; **Anna Wawrzaszek:** conceptualization, methodology, validation, writing – original draft, writing – review and editing; **Emil Wrzosek:** methodology, resources, writing – review and editing; **Edyta Woźniak:** conceptualization, methodology; writing – review and editing; **Szymon Sala:** conceptualization, methodology, investigation, validation; **Marek Ruciński:** conceptualization methodology, validation; **Małgorzata Jenerowicz-Sanikowska:** conceptualization, methodology; **Andrzej Norbert Affek:** conceptualization, methodology, data curation, formal analysis, funding acquisition, investigation, methodology, project administration, resources, supervision, validation, writing – original draft, writing – review and editing.

All authors contributed critically to the drafts and gave final approval for publication.

References

Akandil, C., Meier, P., Otaru, O. & Joshi, J. (2021). Mapping invasive Giant Goldenrod (Solidago gigantea) with multispectral images acquired by unmanned aerial vehicle. *Journal of Digital Landscape Architecture*, **6**, 245–256. https://doi.org/10.14627/537705021

Biró, L., Kozma-Bognár, V. & Berke, J. (2024) Comparison of RGB Indices used for Vegetation Studies based on Structured Similarity Index (SSIM). *Journal of Plant Science and Phytopathology*, **8**, 007-012. https://doi.org/10.29328/journal.jpsp.1001124

Bolch, E.A., Santos, M.J., Ade, C., Khanna, S., Basinger, N.T., Reader, M.O. & Hestir E.L. (2020) Remote Detection of Invasive Alien Species. In: J. Cavender-Bares et al. (eds.), *Remote Sensing of Plant Biodiversity*, 267–307. https://doi.org/10.1007/978-3-030-33157-3_12

Breiman, L. (2001) Random Forests. *Machine Learning* **45**, 5–32. https://doi.org/10.1023/A:1010933404324

Chadoulis, R., Ruciński, M., Katsikis, E., Archicinski, P., Sala, S., Gromny, E., Woźniak, E., Manakos, I., Affek, A. & Foks-Ryznar, A. (2023) Phenological Metrics Derived From Sentinel-2 Data For Solidago Gigantea Mapping. In: IGARSS 2023 - 2023 IEEE International Geoscience and Remote Sensing Symposium, Pasadena, CA, USA, 445–447. https://doi.org/10.1109/IGARSS52108.2023.10282732

de Sá, N.C., Castro, P., Carvalho, S., Marchante, E., López-Núñez, F.A. & Marchante, H. (2018) Mapping the Flowering of an Invasive Plant Using Unmanned Aerial Vehicles: Is There Potential for Biocontrol Monitoring? *Frontiers in Plant Science*, **9**, 293. https://doi.org/10.3389/fpls.2018.00293

586 Dvořák, P., Müllerová, J., Bartaloš, T. & Brůna, J. (2015) Unmanned aerial vehicles for alien
587 plant species detection and monitoring. *The International Archives of the*
588 *Photogrammetry, Remote Sensing and Spatial Information Sciences*, **XL-1/W4**, 83–90.
589 https://doi.org/10.5194/isprsarchives-XL-1-W4-83-2015
590 Haralick, R.M., Shanmugam, K. & Dinstein, I. (1973) Textural features for image
591 classification, *IEEE Transactions on Systems, Man, and Cybernetics,* 3(6), 610–621.
592 https://doi.org/10.1109/TSMC.1973.4309314
593 Hill, D.J., Tarasoff, C., Whitworth, G.E., Baron, J., Bradshaw, J.L. & Church, J.S. (2017).
594 Utility of unmanned aerial vehicles for mapping invasive plant species: a case study on
595 yellow flag iris (*Iris pseudacorus* L.). *International Journal of Remote Sensing*, **38**,
596 2083–2105. https://doi.org/10.1080/01431161.2016.1264030
597 IMGW-PIB. (2025). Klimat Polski 2024. IMGW-PIB. https://imgw.pl/wp-
598 content/uploads/2025/07/RAPORT-IMGW-PIB-Klimat-Polski-2024.pdf
599 Ishii, J. & Washitani, I. (2013) Early detection of the invasive alien plant Solidago altissima
600 in moist tall grassland using hyperspectral imagery. *International Journal of Remote*
601 *Sensing*, **34**, 5926–5936. https://doi.org/10.1080/01431161.2013.799790
602 Kabuce, N. & Priede N. (2010) NOBANIS - Invasive alien species fact sheet - *Solidago*
603 *canadensis*. In: Online database of the European Network on Invasive Alien Species -
604 NOBANIS. www.nobanis.org [Accessed on 11.03.2025]
605 Koco, Š., Dubravská, A., Vilček, J. & Gruľová, D. (2021). *Geospatial Approaches to*
606 *Monitoring the Spread of Invasive Species of Solidago spp. Remote Sensing*, *13*(23),
607 4787. https://doi.org/10.3390/rs13234787
608 Kvile, K.Ø., Gundersen, H., Poulsen, R.N., Sample, J. E., Salberg, A.-B., Ghareeb, M.E.,
609 Buls, T., Bekkby, T. & Hancke, K. (2024). Drone and ground-truth data collection,

610 image annotation and machine learning: A protocol for coastal habitat mapping and
611 classification. *MethodsX*, 13, 102935. https://doi.org/10.1016/j.mex.2024.102935
612 Ledger, K.J., Pal, R.W., Murphy, P., Nagy, D.U., Filep, R. & Callaway, R.M. (2015) Impact
613 of an invader on species diversity is stronger in the non-native range than in the native
614 range. *Plant Ecology*, **216**, 1285–1295. https://doi.org/10.1007/s11258-015-0508-2
615 Lu, B. & He, Y. (2017) Species classification using Unmanned Aerial Vehicle (UAV)-
616 acquired high spatial resolution imagery in a heterogeneous grassland. *ISPRS Journal of*
617 *Photogrammetry and Remote Sensing*, **128**, 73–85.
618 https://doi.org/10.1016/j.isprsjprs.2017.03.011
619 Rizaludin Mahmud, M., Numata, S. & Hosaka, T. (2020) Mapping an invasive goldenrod of
620 Solidago altissima in urban landscapes of Japan using multi-scale remote sensing and
621 knowledge-based classification. *Ecological Indicators*, **111**, 105975.
622 https://doi.org/10.1016/j.ecolind.2019.105975
623 Müllerová, J., Brůna, J., Bartaloš, T., Dvořák, P., Vítková, M. & Pyšek, P. (2017) Timing is
624 important: Unmanned aircraft vs. satellite imagery in plant invasion monitoring.
625 *Frontiers in Plant Science*, **8**, 887. Available from:
626 https://doi.org/10.3389/fpls.2017.00887
627 Musiał, K., Pagitz, K., Gudžinskas, Z., Łazarski, G. & Pliszko, A. (2020) Chromosome
628 numbers in hybrids between invasive and native Solidago (Asteraceae) species in
629 Europe. *Phytotaxa*, **471**, 267–275. https://doi.org/10.11646/phytotaxa.471.3.8
630 Nowak, M.M., Dziob, K., & Bogawski, P. (2018) Unmanned Aerial Vehicles (UAVs) in
631 environmental biology: A Review. *European Journal of Ecology*, **4**, 56–74. Available
632 from: https://doi.org/10.2478/eje-2018-0012

633 Peel, M.C., Finlayson, B.L. & McMahon, T.A. (2007) Updated world map of the Köppen-
634 Geiger climate classification. *Hydrology and Earth System Sciences*, **11**, 1633–1644.
635 https://doi.org/10.5194/hess-11-1633-2007
636 Pejchar, L. & Mooney, H.A. (2009) Invasive species, ecosystem services and human well-
637 being. *Trends in Ecology & Evolution*, **24**, 497–504.
638 https://doi.org/10.1016/j.tree.2009.03.016
639 Pyšek, P. & Richardson, D.M. (2010) Invasive Species, Environmental Change and
640 Management, and Health. *Annual Review of Environment and Resources*, **35**, 25–55.
641 http://dx.doi.org/10.1146/annurev-environ-033009-095548
642 Rakgoale, P.B. & Ngetar, S.N. (2024) Detecting invasive alien plant species using remote
643 sensing, machine learning and deep learning. *Journal of Sensors*, **2024**, 8854675,
644 https://doi.org/10.1155/2024/8854675
645 Regulska, E., Zarzycka, M.A., Obidziński, A., Kołaczkowska, E., Kowalska, A., Jabs-
646 Sobocińska, Z., Wolski, J., Omeliańska, B. & Affek, A.N. (2026) Assessing global
647 trends, biases, and knowledge gaps in research on ecological interactions in goldenrod
648 (Solidago spp.) invasions. *NeoBiota*, **105**, 153–175.
649 https://doi.org/10.3897/neobiota.105.165501
650 R Core Team. (2022) R: A language and environment for statistical computing [Software]. R
651 Foundation for Statistical Computing. https://www.R-project.org/
652 Sabat-Tomala, A., Raczko, E. & Zagajewski, B. (2020) Comparison of Support Vector
653 Machine and Random Forest Algorithms for Invasive and Expansive Species
654 Classification Using Airborne Hyperspectral Data. *Remote Sensing*, **12**(3), 516.
655 https://doi.org/10.3390/rs12030516

Sabat-Tomala, A., Raczko, E. & Zagajewski, B. (2022) Mapping Invasive Plant Species with Hyperspectral Data Based on Iterative Accuracy Assessment Techniques. *Remote Sensing*, **14**, 64. https://doi.org/10.3390/rs14010064

Schmid, B. & Bazzaz, F.A. (1990) Plasticity in Plant Size and Architecture in Rhizome-Derived vs. Seed-Derived Solidago and Aster. *Ecology*, **71,** 523–535. https://doi.org/10.2307/1940306

Singh, K.K., Surasinghe, T.D. & Frazier, A.E. (2024). Systematic review and best practices for drone remote sensing of invasive plants. *Methods in Ecology and Evolution*, 15, 998–1015. https://doi.org/10.1111/2041-210X.14330

Szymura, M. & Szymura, T.H. (2016a) Interactions between alien goldenrods (*Solidago* and *Euthamia* species) and comparison with native species in Central Europe. *Flora-Morphology, Distribution, Functional Ecology of Plants* **218**, 51–61. https://doi.org/10.1016/j.flora.2015.11.009

Szymura, M. & Szymura, T.H. (2016b) Historical contingency and spatial processes rather than ecological niche differentiation explain the distribution of invasive goldenrods (Solidago and Euthamia). *Plant Ecology*, **217**, 565–582. https://doi.org/10.1007/s11258-016-0601-1

Szymura, M., Szymura, T.H. & Wolski, K. (2016) Invasive *Solidago* species: How large area do they occupy and what would be the cost of their removal? *Polish Journal of Ecology* **64,** 25–34. https://doi.org/10.3161/15052249PJE2016.64.1.003

Szymura, M., Szymura, T.H., Rajsz, A. & Świerszcz, S. (2019) Is phenotypic plasticity an explanation for the invasiveness of goldenrods (Solidago and Euthamia) in Europe? *Plant Species Biology* **34**, 73–84. https://doi.org/10.1111/1442-1984.12236

Tokarska-Guzik, B. (2001) The history of studies of invasive alien plants in Poland. In: Tokarska-Guzik, B., Brundu, G., Brock, J., Camarda, I., Child, L., Wade, M. (Eds.),

681 Plant Invasions: Species Ecology and Ecosystem Management. Backhuys Publishers,
682 Leiden, The Netherlands, 245–254.
683 Weber, E. (1998) The dynamics of plant invasions: a case study of three exotic goldenrod
684 species (*Solidago* L.) in Europe. *Journal of Biogeography*, **25,** 147–154.
685 https://doi.org/10.1046/j.1365-2699.1998.251119.x
686 Weber, E. (2003) Invasive Plant Species of the World. A Reference Guide to Environmental
687 Weeds. CABI Publishing, Oxon, UK.
688 Weber, E. & Jacobs, G. (2005) Biological flora of central Europe: Solidago gigantea Aiton.
689 Flora-Morphology, Distribution, *Functional Ecology of Plants*, **200**, 109–118.
690 https://doi.org/10.1016/j.flora.2004.09.001
691 Zagajewski, B., Kluczek M., Zdunek, K.B. & Holland, D. (2024) Sentinel-2 versus
692 PlanetScope Images for Goldenrod Invasive Plant Species Mapping. *Remote Sensing*,
693 **16**, 636. https://doi.org/10.3390/rs16040636

Kołaczkowska, E., Omeliańska, B., Kowalska, A., Zarzycka, M., Regulska, E., Jarocińska, A., Kycko, M., Foks-Ryznar, A., Wawrzaszek, A., Wrzosek, E., Woźniak, E., Sala, S., Ruciński, M., Jenerowicz-Sanikowska, M. & Affek, A.N.

Building a representative UAV RGB reference dataset for national-scale satellite mapping of invasive goldenrods (*Solidago* spp.): an efficient workflow and accuracy drivers

Supporting information

Table S1. Field data sheet (consisting of three consecutive pages) used for the field survey. Land-cover types (on the PAGE 1) were distinguished based on the classification proposed by Skokanová et al (2024): Skokanová, K., Španiel, S., Šingliarová, B., Mereďa, P.Jr., Hodálová, I. & Svitok, M. (2024) Contrasting invasion patterns of two closely related *Solidago* alien species. *Journal of Biogeography*, 51, 1679–1692. https://doi.org/10.1111/jbi.14785

FIELD DATA SHEET – PAGE 1 (BASIC INFORMATION)

This field data sheet is part of the SolidES project: Countrywide mapping of goldenrod invasion and assessing its impact on ecosystems and human well-being, funded by Poland's Ministry of Science and Higher Education; If you find this *sheet*, please contact me *as soon as possible [phone no.]*

Site ID	Completed by [author's initials]	Date	Daily site number
Location [administrative units]			
Arrival time [HH:MM] :		Departure time [HH:MM] :	
Altitude: m a.s.l., Latitude: , Longitude:			

SITE DESCRIPTION

Land-cover type[a]	Ongoing management[b]	*Solidago* species[c] and abundance[d]
1.		
2.		
3.		
4.		
5.		
6.		

[a] **forest/shrubs/forest margin/tree plantation/fallow land/field or grassland margin/alluvial or humid grassland/mesophilic grassland/dry grassland/roadside/railway/quarry or mining heap/ruderal site/dump/waste place/riparian vegetation/dams/embankments**

[b] **no**/**partial** (or irregular)/**regular** (treatments at least 1x/year)

[c] **C** = S. can; **G** = S. gig.

[d] **1** single; **2** up to 100 clumps or one polycormon ϕ <10 m; **3** >100 clumps or polycormon/s ϕ >10 m

Average *Solidago* height [m] [by species]

Additional UAV imagery/videos

YES/NO

Ground-level photographs/videos [authors' names]

FLIGHT & MISSION LOG

UAV Pilot name

Mission dimensions m × m

Mission area ha

Number of waypoints

Flight duration min s

Flight horizontal speed m s^{-1}

Cloud cover [oktas]

[0–8; increasing(↑)/decreasing(↓)]

Sun visibility full/partial/not visible

Camera white balance setting  

Battery ID number

Battery level before takeoff %

Check-in confirmed

Takeoff time [HH:MM] :

Landing time [HH:MM] :

Battery level after landing %

Check-out confirmed

Flight disruptions, technical malfunctions [specify if any]

Landscape and soil characteristics

Additional remarks

[continued on the next page]

FIELD DATA SHEET – PAGE 2 (PLANT SPECIES LIST)

This field data sheet is part of the SolidES project: Countrywide mapping of goldenrod invasion and assessing its impact on ecosystems and human well-being, funded by Poland's Ministry of Science and Higher Education; If you find this *sheet*, please contact me as soon as possible*: [phone no.]*

Site ID	Date	Daily site no.
Plant species identified by [name]:		
Plant species co-occurring with *Solidago*	Land-cover type [1-6]	Additional remarks
1.		
2.		
3.		
4.		
5.		
6.		
7.		
8.		
9.		
10.		
11.		
12.		
13.		
14.		
15.		
Dominant tree and shrub species in the mapping area		
1.		
2.		
3.		
4.		
5.		
6.		
7.		
8.		
9.		
10.		

[continued on the next page]

FIELD DATA SHEET – PAGE 3 (SCHEMATIC SITE PLAN, INCL. LOCATION OF LAND-COVER TYPES, ADDITIONAL INFORMATION)

This field data sheet is part of the SolidES project: Countrywide mapping of goldenrod invasion and assessing its impact on ecosystems and human well-being, funded by Poland's Ministry of Science and Higher Education; If you find this *sheet*, please contact me as soon as possible*: [phone no.]*

Site ID	Date	Daily site no.
Drawing by [name]:		

Table S2. Spectral indices and GLCM-based texture metrics used as additional predictor layers for Random Forest classification of the UAV-derived RGB orthomosaics. **This table is provided as a separate spreadsheet file.**

Table S3. Spectral indices and GLCM-based texture metrics used as additional predictor layers for Random Forest classification of the UAV-derived RGB orthomosaics; *P*(i) – the probability of occurrence of pixel value, *R* – Red Band, *G* – Green Band, *B* – Blue Band.

Name	**Formula**	**Reference**
Triangular Greenness Index (TGI)	$G - 0.39 * R - 0.61 * B$	Hunt, et al. 2013
Brightness Index (BI)	$(R^2 + B^2 + G^2)/3^2$	Richardson, et al. 1977
Vegetative Index (VEG)	$G/(R^{0.667} * B^{0.334})$	Hague, et al. 2006
Blue Chromatic Coordinate Index (BCC)	$B/(R + G + B)$	De Swaef, et al. 2021
Visible NDVI (vNDVI)	$0.5266 * (R^{-0.1294} * G^{0.3389} * B^{-0.3118})$	Costa, et al. 2020
Colour Index of Vegetation (CIVE)	$0.441R - 0.881G + 0.385B + 18.78745$	Kataoka et al. 2003
Principal Component Analysis Index (IPCA)	$0.994 * \lvert R - B\rvert + 0.961 * \lvert G - B\rvert + 0.914 * \lvert G - R\rvert$	Saberioon, et al. 2014
Modified Green Red Vegetation Index (MGRVI)	$(G^2 - R^2)/(G^2 + R^2)$	Bending, et al. 2015
contrast (GLCM)	$\sum_{i=1}^{N_g}\sum_{j=1}^{Ng} P(i,j)(i-j)^2$	Haralick et al. 1973
entropy (GLCM)	$\sum_{i=1}^{N_g}\sum_{j=1}^{Ng} P(i,j)\log(P(i,j))$	Haralick et al. 1973
homogeneity (GLCM)	$\sum_{i=1}^{N_g}\sum_{j=1}^{Ng} \frac{1}{1+(i-j)^2} P(i,j)$	Haralick et al. 1973

References to Table S3:

Bendig, J., Yu, K., Aasen, H., Bolten, A., Bennertz, S., Broscheit, J., Gnyp, M.L. & Bareth, G. (2015) Combining UAV-based plant height from crop surface models, visible, and near infrared vegetation indices for biomass monitoring in barley. International Journal of Applied Earth Observation and Geoinformation, 39, 79–87. https://doi.org/10.1016/j.jag.2015.02.012

Costa, L., Nunes, L. & Ampatzidis, Y. (2020) A new visible band index (vNDVI) for estimating NDVI values on RGB images utilizing genetic algorithms. Computers and Electronics in Agriculture, 172, 105334. https://doi.org/10.1016/j.compag.2020.105334

De Swaef, T., Maes, W.H., Aper, J., Baert, J., Cougnon, M., Reheul, D., Steppe, K., Roldán-Ruiz, I. & Lootens, P. (2021) Applying RGB- and Thermal-Based Vegetation Indices from UAVs for High-Throughput Field Phenotyping of Drought Tolerance in Forage Grasses. Remote Sensing, 13(1), 147. https://doi.org/10.3390/rs13010147

Hague, T., Tillett, N.D. & Wheeler, H. (2006) Automated crop and weed monitoring in widely spaced cereals. Precision Agriculture, 7(1), 21–32. https://doi.org/10.1007/s11119-005-6787-1

Haralick, R.M., Shanmugam, K. & Dinstein, I. (1973) Textural features for image classification. IEEE Transactions on Systems, Man, and Cybernetics, 3(6), 610–621. https://doi.org/10.1109/TSMC.1973.4309314

Hunt, E.R., Doraiswamy, P.C., McMurtrey, J.E., Daughtry, C.S.T., Perry, E.M. & Akhmedov, B. (2013) A visible band index for remote sensing leaf chlorophyll content at the canopy scale. International Journal of Applied Earth Observation and Geoinformation, 21, 103–112. https://doi.org/10.1016/j.jag.2012.07.020

Kataoka, T., Kaneko, T., Okamoto, H. & Hata, S. (2003) Crop growth estimation system using machine vision. In Proceedings of the 2003 IEEE/ASME International Conference on Advanced Intelligent Mechatronics, 2, 1079–1083.

Richardson, A.J. & Wiegand, C.L. (1977) Distinguishing vegetation from soil background information. Photogrammetric Engineering and Remote Sensing, 43. https://ntrs.nasa.gov/citations/19780033290

Saberioon, M.M., Amin, M.S.M., Anuar, A.R., Gholizadeh, A., Wayayok, A. & Khairunniza-Bejo, S. (2014) Assessment of rice leaf chlorophyll content using visible bands at different growth stages at both the leaf and canopy scale. International Journal of Applied Earth Observation and Geoinformation, 32, 35–45. https://doi.org/10.1016/j.jag.2014.03.018

Figures S1–S11. Ground-level photographs supplementing Figures 3–4 and Table 2.

The following figures present selected ground-level photographs taken during the 2024 field survey in Poland by the following authors:

AK – Anna Kowalska

EK – Ewa Kołaczkowska

MZ – Martyna Zarzycka

The captions include figure numbers of the relevant UAV image shown in Figures 3 and 4, and the initials of the photograph's author.

Figure S1. Ground-level photograph supporting Figure 3o (in the main article text); Author: EK.

Figure S2. Ground-level photograph supporting Figure 3s (in the main article text); Author: AK.

Figure S3. Ground-level photograph supporting Figure 4e (in the main article text); Author: EK.

Figure S4. Ground-level photograph supporting Figure 4f (in the main article text); Author: EK.

Figure S5. Ground-level photograph supporting Figure 4i (in the main article text); Author: EK.

Figure S6. Ground-level photograph supporting Figure 4j (in the main article text); Author: MZ.

Figure S7. Ground-level photograph supporting Figure 4k (in the main article text); Author: EK.

Figure S8. Ground-level photograph supporting Figure 4m (in the main article text); Author: EK.

Figure S9. Ground-level photograph supporting Figure 4o (in the main article text); Author: EK.

Figure S10. Ground-level photograph supporting Figure 4r (in the main article text); Author: EK.

Figure S11. Ground-level photograph supporting Figure 4t (in the main article text); Author: EK.

Kołaczkowska, E., Omeliańska, B., Kowalska, A., Zarzycka, M., Regulska, E., Jarocińska, A., Kycko, M., Foks-Ryznar, A., Wawrzaszek, A., Wrzosek, E., Woźniak, E., Sala, S., Ruciński, M., Jenerowicz-Sanikowska, M. & Affek, A.N.

Building a representative UAV RGB reference dataset for national-scale satellite mapping of invasive goldenrods (Solidago spp.): an efficient workflow and accuracy drivers

Supporting information

Table S2. Selected properties of UAV-mapped sites during the field study across Poland in 2024 and the results of RF-classification of the orthophotomaps (classes: *Solidago*: for monospecific invasive goldenrod stands, and Other: for the background, i.e., other vegetation than invasive goldenrods, bare soil, and other features in the landscape); UA - User's Accuracy, PA - Producer's Accuracy; flight height: 100 m AGL.

No	Site name (based on the name of the nearest settlement)	Longitude [decimal degrees]	Latitude [decimal degrees]	Altitude [m a.s.l.]	Date (all dates in year 2024) [day month]	Mission start time (CEST) [HH:MM]	Mission end time (CEST) [HH:MM]	SolarNoon Dist [h]	Days from field survey start	Sky cover [oktas]	Sun visibility [full/partial/not visible]	Dominating cloud level [high/middle/low /no clouds]	Orthomosaic area [ha]	Deep shadows*	Disturbances (mowing)*	Deciduous trees and/or shrubs*	UA *Solidago*	PA *Solidago*	F1-score *Solidago*	UA Other	PA Other	F1-score Other	Mean F1-score *Solidago* and Other
1	Zmyślona Ligocka	17.74370498	51.40102340	190.358	06 Aug	12:19	12:25	0.933	1	4	full, partial	middle	12.39	1	2b	2b	0.887	0.929	0.907	0.990	0.984	0.987	0.947
2	Domasławice	17.54294164	51.40547340	192.104	06 Aug	13:56	14:02	0.683	1	3	full	middle	11.39	1	3	2a	0.953	0.973	0.963	0.990	0.983	0.987	0.975
3	Łazy Małe	17.27310287	51.39595949	183.826	06 Aug	16:09	16:15	2.900	1	3	full	middle	13.23	1	0	2a	0.909	0.911	0.910	0.933	0.931	0.932	0.921
4	Czeszów	17.21220342	51.38598165	158.926	06 Aug	17:48	17:51	4.550	1	1	full	high	6.00	2a	3	2b	0.818	0.854	0.835	0.871	0.845	0.858	0.847
5	Wodnica	16.49463276	51.37770240	131.395	07 Aug	10:19	10:25	2.933	2	2	full	high	13.28	2a	0	3	0.844	0.901	0.872	0.941	0.904	0.922	0.897
6	Ścinawa	16.42891571	51.40256272	94.500	07 Aug	12:44	12:49	0.517	2	0	full	no clouds	11.86	1	3	2b	0.718	0.806	0.760	0.964	0.943	0.953	0.857
7	Szklary Dolne	16.05970513	51.43491517	183.593	07 Aug	14:51	14:55	1.600	2	1	full, partial	high	8.24	1	3	2a	0.886	0.933	0.909	0.983	0.969	0.976	0.943
8	Nowa Kuźnia	15.81737124	51.37996448	183.005	07 Aug	16:35	16:40	3.333	2	3	full, partial	high	9.31	1	2b	2a	0.647	0.724	0.684	0.927	0.898	0.912	0.798
9	Dłużyna Górna	15.13654490	51.22233527	241.596	07 Aug	18:38	18:44	5.383	2	6	full, partial	middle	15.45	1	2a	2a	0.912	0.918	0.915	0.951	0.948	0.949	0.932
10	Oleszna Podgórska	15.46752963	51.03440737	369.401	08 Aug	10:44	10:51	2.517	3	7, 8	partial, not visible	low	11.07	1	2b	3	0.783	0.858	0.819	0.970	0.951	0.960	0.890
11	Jelenia Góra	15.65222943	50.86240466	390.860	08 Aug	12:12	12:16	1.050	3	7	full, partial	middle, low	7.10	1	2b	2a	0.858	0.827	0.842	0.950	0.960	0.955	0.899
12	Krępna	18.06537921	50.44776025	211.033	09 Aug	11:10	11:12	2.083	4	2	full	high	6.24	2a	3	2a	0.652	0.855	0.740	0.984	0.951	0.967	0.853
13	Tarnowskie Góry	18.83813215	50.42187569	350.299	09 Aug	14:17	14:21	1.033	4	3	full	high	7.19	1	2a	3	0.770	0.824	0.796	0.929	0.904	0.916	0.856
14	Chruszczobród	19.32192016	50.41130367	361.701	09 Aug	17:48	17:57	4.550	4	4	full, partial	high	17.05	1	3	2a	0.782	0.835	0.808	0.939	0.916	0.928	0.868
15	Siewierz	19.21145549	50.46872720	345.506	10 Aug	8:47	8:58	4.467	5	7	full, partial	high	17.20	2b	2a	2a	0.832	0.900	0.864	0.970	0.946	0.958	0.911
16	Częstochowa	19.01887021	50.77655915	303.278	10 Aug	10:22	10:34	2.883	5	7	partial	high, middle	17.69	1	3	2b	0.630	0.838	0.719	0.987	0.961	0.974	0.846
17	Czubrowice	19.72066514	50.21541942	482.912	13 Aug	9:44	9:49	3.517	8	2	full	high	14.71	1	2a	1	0.820	0.869	0.844	0.968	0.955	0.962	0.903
18	Czubrowice-2	19.71353320	50.21362073	475.763	13 Aug	10:37	10:42	2.633	8	1	full	high	8.57	1	3	2a	0.740	0.839	0.787	0.965	0.938	0.952	0.869
19	Gromiec	19.30901808	50.05090679	268.493	13 Aug	13:20	13:35	0.083	8	2	full	high	25.34	1	2b	1	0.762	0.898	0.824	0.984	0.956	0.970	0.897
20	Kraków	19.89697760	49.99162334	276.094	13 Aug	16:31	16:36	3.267	8	0	full	no clouds	8.15	2a	2a	3	0.870	0.875	0.873	0.899	0.895	0.897	0.885
21	Wola Rzędzińska	21.10671328	50.03934540	260.615	14 Aug	9:54	9:59	3.350	9	0	full	no clouds	8.70	2a	2a	2a	0.965	0.979	0.972	0.986	0.977	0.982	0.977
22	Trześń	21.66313017	50.24794492	252.307	14 Aug	12:26	12:30	0.817	9	0	full	no clouds	7.55	2a	3	2b	0.933	0.942	0.937	0.976	0.972	0.974	0.956
23	Banachy	22.53368117	50.49549571	216.053	14 Aug	16:54	17:09	3.650	9	0	full	no clouds	19.45	2b	3	3	0.808	0.854	0.830	0.956	0.940	0.948	0.889
24	Przędzel	22.21522375	50.48432431	191.890	15 Aug	9:28	9:42	3.783	10	2	full	high	24.12	2a	2a	2b	0.900	0.887	0.894	0.949	0.956	0.952	0.923
25	Kosin	21.91142373	50.80830006	174.613	15 Aug	12:00	12:10	1.250	10	2	full	high	18.52	2a	2b	2b	0.915	0.937	0.926	0.972	0.962	0.967	0.946
26	Kunów	21.29411380	50.95954680	214.388	15 Aug	14:25	14:28	1.167	10	3	full	high	6.26	1	2a	2a	0.793	0.855	0.823	0.947	0.921	0.934	0.878
27	Trzebiatów	15.32135791	54.05743254	50.334	22 Aug	10:30	10:35	2.750	17	8	not visible	low	7.79	0	2a	4	0.918	0.952	0.935	0.965	0.940	0.952	0.944
28	Gryfice	15.22814078	53.93059940	52.587	22 Aug	13:06	13:21	0.150	17	8	not visible	low	30.57	0	0	2b	0.926	0.972	0.949	0.995	0.986	0.991	0.970
29	Nowogard	15.14019674	53.67299491	90.049	22 Aug	15:05	15:13	1.833	17	7	not visible	low	14.68	0	4	1	0.848	0.835	0.841	0.944	0.949	0.946	0.894
30	Szczecin	14.71635914	53.38473163	43.538	22 Aug	16:56	17:02	3.683	17	5	full, partial	middle	10.79	2b	0	2b	0.798	0.888	0.841	0.964	0.930	0.946	0.894
31	Gorzów	15.28466977	52.76081429	108.169	23 Aug	14:20	14:32	1.083	18	6	partial	high	20.07	1	2a	2a	0.924	0.921	0.923	0.963	0.964	0.964	0.943
32	Świebodzin	15.52044199	52.26272799	149.472	23 Aug	16:19	16:26	3.067	18	4	full, partial	high	19.15	1	2a	2a	0.950	0.969	0.959	0.976	0.961	0.968	0.964
33	Zbąszyń	15.95126605	52.24889692	97.300	23 Aug	18:22	18:25	5.117	18	5	full, partial	high	8.62	1	3	3	0.784	0.871	0.826	0.959	0.926	0.942	0.884
34	Pieńki Słubickie	20.60200820	51.99864711	193.110	26 Aug	10:18	10:22	2.950	21	7	partial, not visible	middle, low	10.50	0	1	3	0.854	0.884	0.869	0.928	0.909	0.918	0.894
35	Stary Łajszczew	20.35448897	51.93647134	192.730	26 Aug	12:14	12:21	1.017	21	6	full, partial	middle	18.92	1	2a	2a	0.861	0.887	0.874	0.962	0.953	0.958	0.916

36	Stryków	19.61146354	51.91359181	199.557	26 Aug	14:03	14:18	0.800	21	5	partial	high, middle, low	27.68	1	0	1	0.866	0.942	0.902	0.992	0.979	0.985	0.944
37	Zgierz	19.37970363	51.88348131	212.191	26 Aug	15:40	15:48	2.417	21	7	partial	middle	14.05	1	0	2a	0.967	0.982	0.975	0.988	0.977	0.982	0.979
38	Pabianice	19.34414256	51.64748853	220.541	27 Aug	10:32	10:42	2.717	22	1	full	high	16.09	2a	3	2a	0.859	0.933	0.895	0.991	0.980	0.985	0.940
39	Włodzimierzów	19.95851983	51.33242159	227.686	27 Aug	12:40	12:46	0.583	22	1	full	high	12.78	1	1	1	0.928	0.980	0.953	0.995	0.979	0.987	0.970
40	Kłudno	20.81189839	51.37742945	200.509	27 Aug	14:57	15:05	1.700	22	3	full	middle	15.73	2a	1	2b	0.869	0.912	0.890	0.957	0.934	0.945	0.918
41	Puławy	21.98313580	51.37969546	157.707	28 Aug	9:47	9:54	3.467	23	0	full	no clouds	16.42	2a	2a	2a	0.825	0.831	0.828	0.935	0.932	0.933	0.881
42	Łuszczów Pierwszy	22.72474134	51.29174339	215.043	28 Aug	12:40	12:46	0.583	23	0	full	no clouds	15.20	1	3	1	0.970	0.967	0.968	0.980	0.982	0.981	0.975
43	Jawidz	22.71387716	51.35644649	205.069	28 Aug	13:57	14:01	0.700	23	3	full, partial	middle	5.66	2a	1	2a	0.859	0.841	0.850	0.944	0.975	0.960	0.905
44	Jawidz-2	22.74205561	51.35240476	184.946	28 Aug	14:55	15:01	1.667	23	5	full	middle	13.55	2a	2a	2a	0.922	0.940	0.931	0.970	0.961	0.966	0.948
45	Liszno-Kolonia	23.09391696	51.10845524	210.595	28 Aug	16:44	16:52	3.483	23	3	full	middle	12.91	3	1	3	0.963	0.974	0.969	0.991	0.987	0.989	0.979
46	Chełm	23.43507123	51.12260002	230.528	29 Aug	8:15	8:20	5.000	24	2	partial	high	9.13	2b	2a	2b	0.808	0.892	0.848	0.947	0.901	0.924	0.886
47	Hredków	23.43494273	51.23281717	208.383	29 Aug	10:25	10:32	2.833	24	0	full	no clouds	12.84	1	2a	2a	0.868	0.911	0.889	0.979	0.968	0.974	0.931
48	Cyców	23.13032145	51.29724124	199.622	29 Aug	11:42	11:49	1.550	24	1	full	high	16.71	1	2a	2a	0.896	0.923	0.909	0.955	0.938	0.946	0.928
49	Głębokie	23.08794691	51.29729674	122.835	29 Aug	12:18	12:24	0.950	24	3	full	high, middle	12.62	2a	2a	2b	0.926	0.976	0.951	0.992	0.973	0.982	0.966
50	Siedlce	22.30279399	52.13726345	184.854	29 Aug	16:56	17:03	3.683	24	2	full	high, middle	15.86	2b	0	2b	0.902	0.931	0.916	0.967	0.952	0.960	0.938
51	Siedlce-2	22.24908228	52.18288700	178.823	29 Aug	17:46	17:53	4.517	24	2	full	high, middle	12.57	3	0	2b	0.841	0.873	0.857	0.946	0.931	0.938	0.897
52	Mrowiska	21.37417715	52.23894825	145.498	30 Aug	9:36	9:46	3.650	25	3	full	high, middle	17.67	2a	2a	2b	0.913	0.940	0.926	0.960	0.941	0.950	0.938
53	Karczew	21.21880411	52.08005106	118.568	30 Aug	10:56	11:05	2.317	25	5	partial	high, middle	17.70	0	0	2b	0.888	0.878	0.883	0.960	0.964	0.962	0.922
54	Góra Kalwaria	21.23820721	51.98284208	198.546	30 Aug	12:33	12:38	0.700	25	3	full	high, middle	13.35	2a	0	2b	0.870	0.798	0.832	0.917	0.949	0.933	0.882
55	Czersk	21.23751557	51.95200511	124.809	30 Aug	13:03	13:09	0.200	25	4	full	high, middle	13.22	2a	1	3	0.734	0.797	0.764	0.944	0.922	0.933	0.848
56	Pohulanka	20.83821676	52.26841370	128.754	03 Sep	8:48	8:54	4.450	29	1	full	high	11.40	2b	2a	2a	0.855	0.838	0.846	0.873	0.886	0.879	0.863
57	Dziekanów Polski	20.84983055	52.37016091	107.197	03 Sep	10:16	10:22	2.983	29	1	full	high	11.99	2b	2a	2b	0.766	0.805	0.785	0.940	0.925	0.932	0.859
58	Nowy Kamion	20.19252120	52.37080528	98.336	03 Sep	11:58	12:04	1.283	29	1	full	high	10.71	2a	1	2a	0.855	0.879	0.867	0.928	0.914	0.921	0.894
59	Płock	19.71666488	52.50797194	90.218	03 Sep	13:21	13:30	0.100	29	1	full	high	13.68	2a	0	2a	0.861	0.834	0.847	0.957	0.965	0.961	0.904
60	Elbląg	19.45613237	54.16265417	96.190	05 Sep	11:24	11:31	1.850	31	5	partial	high	13.50	1	0	2a	0.956	0.963	0.959	0.939	0.929	0.934	0.947
61	Elbląg-2	19.42472843	54.20334033	107.801	05 Sep	12:51	12:56	0.400	31	4	partial	high	9.09	2a	1	2a	0.786	0.857	0.820	0.968	0.948	0.958	0.889
62	Ostróda	20.00245884	53.69350245	130.004	05 Sep	15:23	15:31	2.133	31	4	full	middle	23.05	2a	0	2b	0.868	0.925	0.896	0.958	0.924	0.941	0.918
63	Podkampinos	20.46178418	52.24350728	120.153	09 Sep	9:41	9:47	3.567	35	3	partial	middle	12.51	2a	2b	2a	0.819	0.682	0.745	0.891	0.872	0.881	0.813
64	Bogdaniec	20.34286908	52.24626477	121.413	09 Sep	10:53	10:58	2.367	35	5	partial	middle	12.81	1	1	2a	0.677	0.731	0.703	0.970	0.917	0.943	0.823
65	Naborów	20.49834400	52.49766527	146.947	09 Sep	13:44	13:49	0.483	35	7	not visible	middle, low	12.67	0	2a	2a	0.969	0.961	0.965	0.974	0.979	0.977	0.971
66	Błędów	20.67230360	52.53334994	119.711	09 Sep	14:46	14:52	1.517	35	8	not visible	middle, low	12.27	0	0	1	0.959	0.959	0.959	0.980	0.980	0.980	0.969
67	Wólka Pęcherska	20.98035844	52.03387388	146.333	11 Sep	9:39	9:50	3.600	37	2	partial	middle	16.74	2b	2a	2b	0.718	0.826	0.769	0.914	0.850	0.881	0.825
68	Łubna	21.13947331	52.03412267	144.105	11 Sep	11:09	11:19	2.100	37	4	partial	middle	15.97	2a	0	2b	0.874	0.875	0.874	0.943	0.942	0.942	0.908
69	Osieck	21.40253040	51.98317006	155.634	11 Sep	13:32	13:39	0.283	37	6	partial	middle	11.73	2a	1	2b	0.810	0.805	0.808	0.860	0.864	0.862	0.835
70	Garwolin	21.64643739	51.89437331	172.845	11 Sep	15:21	15:29	2.100	37	3	full	middle	18.78	2a	2a	2b	0.814	0.752	0.782	0.918	0.942	0.930	0.856
71	Jamielne-bis	21.90087026	51.97635963	194.749	12 Sep	10:28	10:37	2.783	38	5	partial	middle	29.02	2a	1	2a	0.917	0.942	0.930	0.987	0.981	0.984	0.957
72	Niwiski	22.15729961	52.21343507	182.653	12 Sep	12:22	12:27	0.883	38	6	partial	middle	10.70	2a	0	2a	0.829	0.910	0.867	0.989	0.978	0.983	0.925
73	Doliwo	22.46765847	52.24934707	195.369	12 Sep	14:05	14:14	0.833	38	7	partial	middle, low	22.64	1	1	2a	0.851	0.902	0.876	0.969	0.950	0.959	0.917
74	Turzyn	21.51245680	52.61316201	131.155	13 Sep	10:29	10:36	2.767	39	8	not visible	low	16.56	0	0	1	0.933	0.928	0.930	0.952	0.955	0.954	0.942
75	Jadów	21.61051568	52.48322723	136.569	13 Sep	11:53	12:02	1.367	39	8	not visible	middle, low	14.16	1	2b	2a	0.934	0.890	0.912	0.841	0.903	0.871	0.891
76	Rudniki	21.51442311	52.39330504	143.604	13 Sep	13:15	13:19	0.000	39	8	not visible	middle, low	7.49	1	2b	2a	0.957	0.954	0.956	0.904	0.910	0.907	0.931
77	Rudniki - Cienka	21.52859966	52.39941272	139.745	13 Sep	14:10	14:14	0.917	39	8	not visible	middle, low	8.47	1	0	2a	0.959	0.939	0.949	0.915	0.941	0.928	0.939
78	Nowe Lipiny	21.27699775	52.34929063	127.871	13 Sep	15:29	15:39	2.233	39	8	not visible	low	15.60	1	0	2a	0.954	0.959	0.957	0.966	0.962	0.964	0.960
79	Ossów	21.22262425	52.31237318	124.846	13 Sep	16:44	16:50	3.483	39	8	not visible	low	10.39	1	2a	2b	0.951	0.925	0.938	0.937	0.958	0.948	0.943
80	Kopanica**	15.91169851	52.10781939	91.814	24 Aug	10:46	10:55	NA	NA	0	full	no clouds	NA	NA	NA	NA	NA	NA	NA	NA	NA	NA	NA

* 5-point cover scale of Braun-Blanquet with additional subclasses 2a and 2b:
1: <5% cover
2: 5%–25% cover (2a: 5%-15%, 2b: 15%-25%)

3: 25%–50% cover
4: 50%–75% cover
5: 75%–100% cover
For calculation purposes, each class was assigned a percentage value corresponding to the middle of the range (2.5, 10, 20, 37.5, 62.5, 87.5, respectively).
Lack of coverage is expressed by the value 0 (zero).

** an additional mapped site, containing no invasive goldenrods, not classified, not considered in the statistical analyses